Hindawi
International Journal of Optics
Volume 2022, Article ID 4182037, 13 pages
https://doi.org/10.1155/2022/4182037

Research Article

Design and Analysis of Ultralow Voltage Graphene on the Silicon Rich Nitride Tunable Ring Resonator-Based Add-Drop Filter for DWDM Systems

Filston Rukerandanga[1], **Stephen Musyoki**[2] **and Edwin O. Ataro**[2]

[1]*Pan African University, Institute of Sciences Technology and Innovation, Juja, Kenya*
[2]*Technical University of Kenya, Nairobi, Kenya*

Correspondence should be addressed to Filston Rukerandanga; filston2006@gmail.com

Received 29 June 2022; Revised 31 October 2022; Accepted 26 November 2022; Published 9 December 2022

Academic Editor: Stefan Wabnitz

We propose and simulate a third-order 3D electro-optically highly tunable compact add-drop filter based on nonlinear microring resonators. The used tuning mechanism relies on enhanced Kerr nonlinearity in a graphene layer integrated on top of a two-photonabsorption-free and low loss silicon-rich nitride core material at telecommunication wavelengths. An ultrahigh tuning efficiency (150 pm/V) over a tuning range of 1.3 nm, ensuring ultralow voltage consumption, was achieved in this work. We used titanium oxide and silicon oxide as the upper-cladding and under-cladding materials, respectively, around the silicon-rich nitride core material, to come up with a polarization-insensitive, and the thermally resilient third-orderadd-drop optical filter in the L band (1565 nm–1625 nm) with a full wave at a half maximum bandwidth of 50 GHz (linewidth of 0.4 nm) around 1570 nm, a high-free spectral range of 18.5 nm, a quality factor of 2580, an extinction ratio of 60 dB, a finesse of 19, and a thermal stability of 0.3 pm/K. A three-dimensional multiphysics approach was used to simulate the propagation of transverse electric and transverse magnetic polarized waves through the filter, combining the electromagnetic features with thermo-optic and stress-optical effects. The contribution of this work to the existing literature is that the designed filter proposes a new and highly tunable material system compatible with the complementary metal-oxide-semiconductor fabrication technology while combining high tunability, polarization insensitivity, and high thermal stability features for an ultracompact and energy-efficienton-chip integrated photonic tunable filter for dense wavelength division multiplexing systems in the less occupied *L* band.

1. Introduction

On-chip silicon photonic integrated devices for the next-generation technologies have attracted great interest where small footprints for ultradense integration, low-power consumption, high-speed data transmission, high efficiency, and ultrafast tuning are highly desired [1, 2]. In that line, ring resonator-based devices such as add-drop filters [3], delay lines [4], all-optical switches [5], high-speed modulators [6], and optical frequency comb generators [7]. have shown their capability in simultaneously addressing challenges such as low drive power, compactness, and a complementary metal-oxide-semiconductor (CMOS)-compatibility in photonic integrated circuits. In the past, particularly for optical filters, different material systems including Si [8], SiN [9], InP/InGaAsP [10], AlN [11], GaAs [12], polymers [13], and chalcogenides [14] have been used to fabricate ring resonator-based devices. The tuning mechanisms investigated in these materials include the thermo-optic effect [15], the electro-absorption effect [16], the electro-optomechanical effect [17], and the electro-optic (EO) effect [1, 18]. Unfortunately, many of the previously mentioned materials suffer from one or many drawbacks and limitations such as low tuning speed and efficiency, temperature and polarization sensitivity, aging, stability, scalability, and large footprint.

For illustration, silicon is an excellent CMOS-compatible material for passive and active ultracompact optical components, but it is challenging to achieve athermal, polarization-insensitive, highly efficient tunable devices using pure silicon material in the near-infrared (IR) at telecommunication wavelengths. The most widely used approach to realize tunable integrated silicon photonic systems is based on the thermal effects in silicon due to its high thermo-optic coefficient (1.8×10^{-4}/K). The tuning efficiency for this method can reach 48.4 mW/nm while dynamic tuning measurement shows that the 10%–90% rise and 90%–10% fall time of the filter are 12.63 and 6.31 μs, respectively, which is quite slow [19]. Additionally, it adds complexity to the device by integrating microheaters [20]. This results in high voltage consumption, which impedes the aim of realizing a compact, fast, and energy-efficient optical device for on-chip photonics.

On top of that, other shortcomings such as high bending losses and polarization rotation due to the strong high index contrast for small ring radius, ring resonators in a Si-SiO_2 material system have pushed the researchers in current photonic technologies to integrate onto the silicon chip low-index contrast III-V compound materials [21] and other materials such as silicon nitride derivatives, glass, and polymers [22], often at the expense of large footprint, CMOS-incompatibility, and the high fabrication cost. Especially, the monolithic integration of III-V compound materials on silicon is impeded by high-production costs and large mismatches in lattice constants and thermal expansion coefficients [23].

To address the thermal dependence, athermal core materials such as Ta_2O_5 materials [24] or top cladding materials with negative thermo-optic coefficients such as titanium dioxide [25, 26], sol-gel materials [27], chalcogenides [14], and polymethyl-methacrylate (PMMA) [28] have previously been used to offset the positive coefficient of the core and substrate materials (Table 1).

Polarization independence can in principle be achieved by carefully balancing material-dependent and geometry-dependent effects. Therefore, to reduce the polarization dependence due to structural birefringence, Si_3N_4, SiON as alternative materials to silicon are reported in the literature [26, 29]. The methods mentioned previously are preferred to the use of polarization diversity schemes or additional compensating functions (polarization rotator and polarization splitter-rotator) [30] that come with extra complexity and additional components.

This work combined the use of a highly electro-optically tunable hybrid graphene-coated core material (Si_3N_4) which exhibits low loss at telecommunication wavelengths and low structural birefringence [31] with proper optimization of the cross-section for polarization-insensitive waveguide. We determined a critical radius for ring resonators to minimize bending losses and polarization rotation. To counter temperature dependence, a top cladding material with a negative thermo-optic coefficient (TiO_2) was used. To enhance the tuning efficiency, a 2D layer of graphene for its unprecedented high Kerr coefficient, high mechanical strength, high flexibility, high optical transparency, high carrier mobility [32], and high responsivity respecting CMOS-compatible processes [33] will be deposited on the top of the core material to realize a tunable, polarization insensitive, and temperature-independent filter while retaining the silicon platform for its low-fabrication cost. As a result, we use the photonic confinement and long-range waveguiding properties of silicon-rich nitride while also leveraging graphene's high optical nonlinearities for electro-optical tuning. Recently, measurements have confirmed that graphene exhibits a strong Kerr nonlinearity [34].

Graphene on a silicon dioxide material system was reported in [35] and is found in a material system with SiO_2 and Si_3N_4 to realize experimentally a tunable delay line [36]. The proposed electrodes for this device are made of titanium nitride (TiN), which has optical properties that are very similar to those of gold, yet, unlike the latter, TiN is CMOS-compatible [23].

The theoretical background of the research work and the methodology used for the proposed model are given in Section 2. Discussion and results of the simulated model are reported in Section 3. Finally, Section 4 provides the final conclusions of the work.

2. Materials and Methods

The materials and methods are as follows:

2.1. Materials. The transfer functions at the drop and through ports were determined to evaluate the response of the filter in the less occupied L band (1565 nm–1625 nm). The coupled mode theory was applied directly on a third-order filter model in Figure 1 and takes into account the amplitude decay rate due to intrinsic loss γ_i, and the decay rates due to coupling from outer microrings to the input and output waveguides, γ_0, and γ_3, related to the ring-to-bus energy coupling coefficients by $\gamma_0 = \mu_0^2/2$ and $\gamma_3 = \mu_3^2/2$. The following differential equations describe the mode coupling in the filter [38]:

$$\begin{aligned}
\frac{da_1}{dt} &= \left(j\omega_1 - \gamma_i - \gamma_0\right) \quad a_1 - j\mu_1 a_2 - j\mu_0 s_i, \\
\frac{da_2}{dt} &= \left(j\omega_2 - \gamma_i\right)_2 - j\mu_1 a_1 - j\mu_2 a_3, \\
\frac{da_3}{dt} &= \left(j\omega_3 - \gamma_i - \gamma_3\right) \quad a_3 - j\mu_2 a_2, \\
s_t &= s_i - j\mu_1 a_1, \\
s_d &= -j\mu_3 a_3.
\end{aligned} \tag{1}$$

The ring-to-ring energy coupling coefficients μ_k can be related to the corresponding field coupling coefficients κ_k through

$$\kappa_k = \frac{\mu_k}{FSR}, \quad 1 \leq k \leq 2. \tag{2}$$

$$\kappa_k = \frac{\mu_k}{\sqrt{FSR}}, \quad k = 0, 3. \tag{3}$$

For ring-to-bus waveguides energy coupling coefficients.

Table 1: Classic materials used in ring resonator-based tunable devices compared with innovative materials on the basis of optical properties to address thermal, polarization, and low tuning efficiency while keeping CMOS-compatibility [27, 37].

Materials	Refractive index	TOC ($\times 10^{-4}$/K)	CTE ($\times 10^{-6}$/K)
SiO_2	1.445	0.1	0.38
Si	3.478	1.8	2.6
Si_3N_4	2.198	0.24	3.0
Polymer	1.3~1.66	−4.5.0~−1.0	200
TiO_2 (Sputtered film)	2.42	−1~2.15	11.8
TiO_2 (Evaporated film)	2.13	−7.0~−3.0	11.8
Sol-gel	1.07~1.5	−3.0~−0.8	—

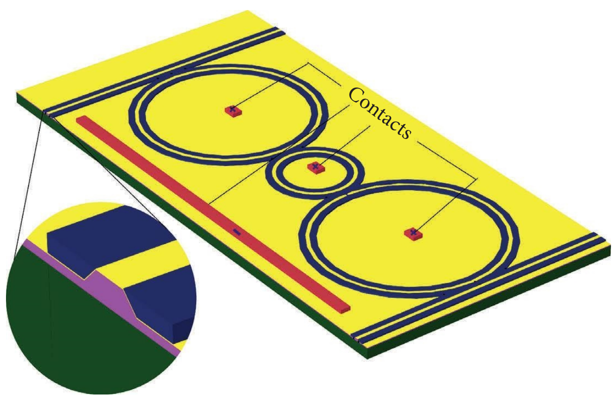

Figure 1: Schematic of the 3D model of the designed filter. The color code for different layers is the same as in Figure 2.

Equations (2) and (3) are then later used to determine the coupling gap distances between the microrings and between the microrings and the bus waveguides using the Bahadori model [15].

However, (1) becomes incapable of describing the interactions between light and matter when nonlinear effects are involved. If the nonlinearities are considered, they will modify the refractive index of the cavity and shifts the central frequency to $\omega_0' = \omega_0 + \delta\omega$. Therefore, the nonlinear perturbation theory is combined with (1) by considering the following corrections $\delta\omega_{NL}$ and $\gamma_{NL} = \mathrm{Im}(\delta\omega)$ as perturbations to the model in (1).

Due to the strong Kerr nonlinearity in graphene and silicon rich nitride [39], it is assumed that the Kerr nonlinearity is the main source of the refractive index change Δn_{NL}^{p}, given by

$$\Delta n_{NL} = n_2^{\mathrm{Kerr}} U, \quad (4)$$

the nonlinear Kerr parameter is given by

$$\gamma_{NL} = \frac{2\pi n_2}{\lambda A_{\mathrm{eff}}}, \quad (5)$$

where n_2 is the Kerr coefficient of graphene. U is the power derived from the applied bias voltage on the electrodes.

A change in effective refractive induces a resonant frequency shift computed using perturbation theory as

$$\Delta\omega_{NL} = \frac{\int_V n\Delta n_{NL} |\overrightarrow{E}|^2 \mathrm{d}V}{\int_\infty n^2 |\overrightarrow{E}|^2 \mathrm{d}V}, \quad (6)$$

where V is the volume of the ring resonator and E is the electric field intensity confined in the ring.

We assume that the ultrafast Kerr effect, relatively low in pure silicon material, is the most dominant phenomenon in graphene [33], while other nonlinearities do not substantially contribute. S_3N_4 is reported to suppress the slow two-photon absorption (TPA) nonlinearity for wavelengths greater than 1.2 μm, which is a source of nonlinear losses at high power [40]. S_3N_4 exhibits a Kerr nonlinearity n_2 of $2.8\times 10^{-7}\,\mathrm{m^2 W^{-1}}$, approximately ten times higher than silicon material [41]. This effect changes the refractive index and thereby shifts the resonant wavelength [38].

Equation (1) is therefore modified to consider the nonlinearities in microring resonators as follows:

$$\begin{aligned}
\frac{da_1}{dt} &= (j\omega_1 + \delta\omega_{NL}(U)) - \gamma_i - \gamma_0 - \gamma_{NL}(U)) \quad a_1 - j\mu_1 a_2 - j\mu_0 s_i, \\
\frac{da_2}{dt} &= (j\omega_2 + \delta\omega_{NL}(U)) - \gamma_i - \gamma_{NL}(U)) \quad a_2 - j\mu_1 a_1 - j\mu_2 a_3, \\
\frac{da_3}{dt} &= (j\omega_3 + \delta\omega_{NL}(U)) - \gamma_i - \gamma_3 - \gamma_{NL}(U)) \quad a_3 - j\mu_2 a_2, \\
s_t &= s_i - j\mu_1 a_1, \\
s_d &= -j\mu_3 a_3.
\end{aligned} \quad (7)$$

The solutions to (7) gives transfer functions of the filter considering a harmonic input wave excitation and harmonic solutions for the wave amplitudes of the form $s_i \sim e^{j\omega t}$ and $a_i \sim e^{j\omega t}$.

Thus, through and drop ports transfer functions of the filter can be expressed, respectively, as

$$\begin{aligned}
H_t &= \frac{s_t}{s_i} = 1 - \frac{j\mu_0 a_1}{s_i} = 1 - \frac{\mu_0^2}{s + \gamma_0 + \mu_1^2/s + \mu_2^2/s + \mu_3^2/s + \gamma_3}, \\
H_d &= \frac{s_d}{s_i} = \frac{-j\mu_3 a_3}{s_i} = \frac{(-j)^4 (\mu_0\mu_1\mu_2\mu_3)}{C_3(s)}.
\end{aligned} \quad (8)$$

The complex centered frequency around the resonant frequency ω_i is written as $s = j(\omega - \omega_i) - \delta\omega_{\mathrm{NL}}(U) + \gamma_i + \gamma_{\mathrm{NL}}(U)$, and $C_3(s)$ is the expression of the denominator in the through-port transfer function. In the following paragraph, we assume that all ring resonators have the same

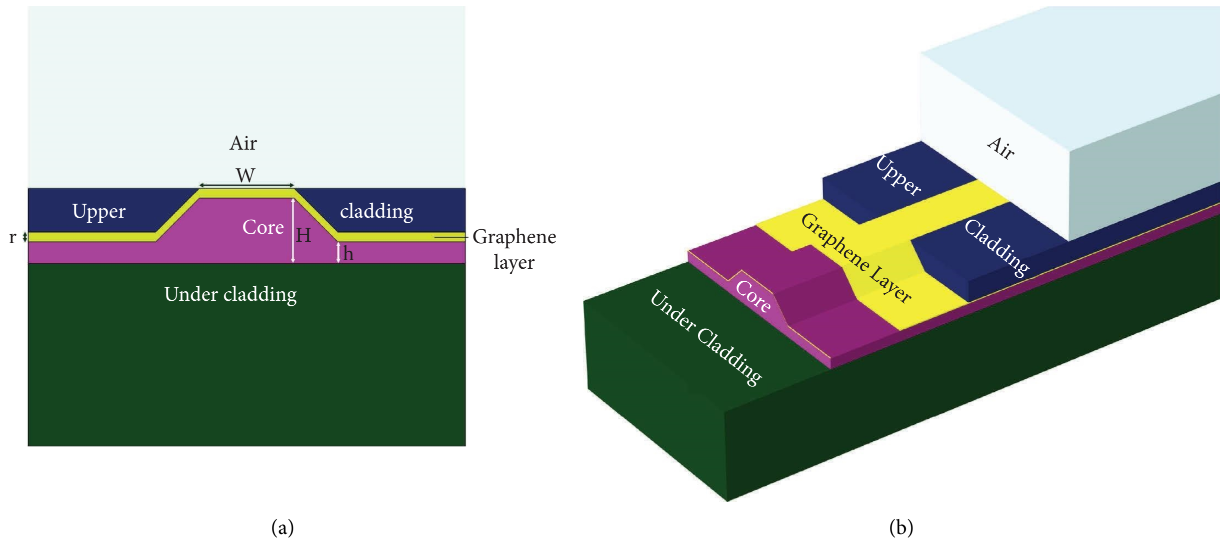

FIGURE 2: (a) Waveguide cross section. (b) Schematic of the different layers of the 3D view of the graphene-coated waveguide. The optimal dimensions of the cross-section are $W = 650$ nm, $H = 75$ nm, $h = 15$ nm, and $r = 3.4$ nm.

resonant frequency as they have the same dimensions and are fabricated in the same material system.

The coupling coefficients for this case of a finite series of microrings must be apodized to mitigate wave reflections that cause large ripples in the passband. Closed formulas can be found for Butterworth filters with a flat-top response in the passband [42, 43]. Their values are given in Table 2.

To increase the tuning range of the filter and to suppress interference with neighboring DWDM channels, the second microring radius is modified to expand the free spectral range (Figures 1 and 3). The resulting device exhibited resonance where the individual resonances of all microrings in the device match [44].

The following step consists of investigating the athermal behavior of the proposed device. The resonant wavelength shift of a microring resonator due to temperature change is given by

$$\frac{d\lambda}{dT} = \frac{\lambda}{n_g}\left(\frac{\partial n_{\text{eff}}}{\partial T} + n_{\text{eff}}\alpha_{\text{sub}}\right), \tag{9}$$

where n_g and α_{sub} are the group indexes of the waveguide and the coefficient of thermal expansion (CTE) of the substrate, respectively. From (9), the athermal condition is achieved when $\partial n_{\text{eff}}/\partial T + n_{\text{eff}}\alpha_{\text{sub}}$ becomes zero, thus $\partial n_{\text{eff}}/\partial T$ has to be negative.

We can reduce the temperature-dependent wavelength shift (TDWS) by adjusting the thickness of under-cladding and upper-cladding materials around the core:

$$n_{\text{eff}} = \Gamma_{\text{core}} n_{\text{core}} + \Gamma_{\text{up}} n_{\text{up}} + \Gamma_{\text{un}} n_{\text{un}}. \tag{10}$$

Γ_{up} and Γ_{un} are the under-cladding and upper-cladding confinement factors, respectively.

$$\frac{\partial n_{\text{eff}}}{\partial T} \approx \Gamma_{\text{core}}\frac{\partial n_{\text{core}}}{\partial T} + \Gamma_{\text{up}}\frac{\partial n_{\text{up}}}{\partial T} + \Gamma_{\text{un}}\frac{\partial n_{\text{un}}}{\partial T}. \tag{11}$$

The zero TDWS condition of the waveguide can then be written as

TABLE 2: Apodized energy coupling coefficients ($\mu(i)$) and field ($\kappa(i)$) coupling coefficients of a 50 GHz-bandwidth and 3.7 nm-FSRthird-order filter.

i	TE		TM	
	$\mu(i)\,[\text{GHz}^{1/2}]$	$\kappa(i)$	$\mu(i)\,[\text{GHz}^{1/2}]$	$\kappa(i)$
0	8.8623	0.34638	8.8623	0.346328
1	27.768	0.042418	27.768	0.042419
2	27.768	0.042418	27.768	0.042419
3	8.8623	0.34638	8.8623	0.346328

$$n_{\text{eff}}\alpha_{\text{sub}} = -\frac{\partial n_{\text{eff}}}{\partial T}. \tag{12}$$

The objective of this study is to use cladding materials with thermo-optic coefficients which have opposite signs in order to come up with an effective TOC that will counterbalance thermo-expansion effects in the device.

In order to realize simultaneously an athermal and polarization-insensitive device, the authors put extra effort into the engineering of the cross-section of the waveguide. When waveguides exhibit different index contrast in vertical and lateral dimensions, polarization independence may be achieved by modifying the height-width ratio of the waveguide or by simply adapting the waveguide width when the index contrast varies in the lateral direction [44].

The geometrical parameters (Figure 2) are optimized to make $n_{\text{eff,TE}} = n_{\text{eff,TM}}$ which is the zero birefringence condition. In addition, the cross-section dimensions should only allow single-mode operation for both orthogonal polarizations. Furthermore, the energy efficiencies should be such as $\kappa_{\text{TE}} = \kappa_{\text{TM}}$ and, apart from increasing losses, the induced stress enhances the polarization sensitivity and index shifts in the waveguide with ring radius reduction. Therefore, a critical radius was computed to minimize such effects.

As mentioned earlier in Section 1, the predominant nonlinearity in Si_3N_4 at telecommunication wavelengths is

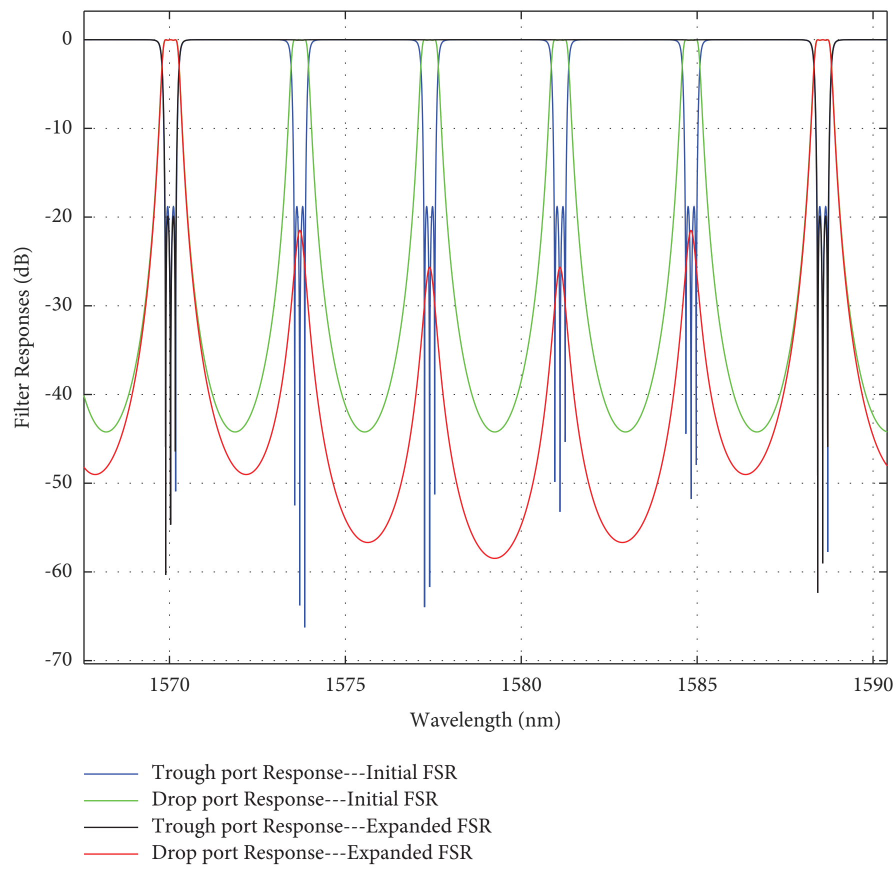

Figure 3: Filter response with an expanded FSR (Vernier effect) from 3.7 nm to 18.5 nm. This avoids the potential interference of neighboring DWDM channels on the full-FSR range.

the Kerr effect. The TPA is absent due to its high band gap. The thermo-optic effects are intended to be suppressed by the application of the athermal condition (12). The ability to efficiently tune Si_3N_4 using the electro-optic (EO) effect is enhanced by depositing a layer of graphene on top of the core to get a material platform cumulating low loss, high nonlinearity, and highly efficient tuning without affecting its optical performance [45].

It is important to put attention to the optical characteristics of the graphene material. The Kubo model describes graphene by defining its surface conductivity (σ) and the complex permittivity (ϵ), from which the refractive index (n) and the extinction coefficient(k) can be calculated [46].

$$\sigma(\omega,\Gamma,\mu_c,T) = \frac{ie^2 k_B T}{\pi\hbar^2(\omega+i2\Gamma)}\left[\frac{\mu_c}{k_B T} + 2\ln\left(e^{-\mu_c/k_B T}+1\right)\right] + \frac{ie^2}{4\pi\hbar}\ln\left[\frac{2|\mu_c|-(\omega+i2\Gamma)}{2|\mu_c|+(\omega+i2\Gamma)}\right], \tag{13}$$

where ω is the angular frequency, Γ is the scattering rate, μ_c is the chemical potential, T is the temperature, e is the charge of the electron, $\hbar \approx 6,582119570 \times 10^{-16}$ eV is the reduced Planck constant, and $k_B = 1.38064852 \times 10^{23}\ \mathrm{JK}^{-1}$, the Boltzmann constant.

The permittivity of graphene can be deducted from (14) using

$$\varepsilon(\omega,\Gamma,\mu_c,T) = 1 + i\frac{\sigma(\omega,\Gamma,\mu_c,T)}{\varepsilon_0\omega\Delta} = \varepsilon_{re} + i\frac{\sigma_{re}(\omega,\Gamma,\mu_c,T)}{\varepsilon_0\omega\Delta}, \tag{14}$$

where ε_0 is the vacuum permittivity, $\varepsilon_{re} = 1 - \sigma_{im}(\omega,\Gamma,\mu_c,T)/\varepsilon_0\omega\Delta$ is the real part of the permittivity [47], and Δ is the layer thickness.

Then, from (14), the complex refractive index is expressed by

$$n + ik = \sqrt{\varepsilon(\omega,\Gamma,\mu_c,T)}. \tag{15}$$

The energy tuning range is determined by considering the surface current on the graphene layer using COMSOL Multiphysics software. When the tuning voltage is applied on TiN electrodes with an equivalent energy close to the the Dirac point (transition point between intraband and interband regions), interband absorption occurs as the electrons are excited by the incident photons. As a result, the graphene layers exhibit high absorption and behave as a lossy medium. When energy is increased up to a value greater than half the photon energy of the incident light, all the electron states in graphene would be filled. As a result, no interband transition is allowed due to Pauli blocking. In this condition, the graphene layers turn to be transparent [48]. Between the two extremes exist a step change region, ($0.2\,\text{eV} < \mu_c < 0.6\,\text{eV}$), suitable for tuning since there is a significant stepping up in the permittivity profile of the graphene layer (Figure 4). This will change the effective index and subsequently shifts the resonant wavelength of the device [46]. When there is no applied voltage ($V_G = 0$), the graphene layers behave as a transparent thin sheet.

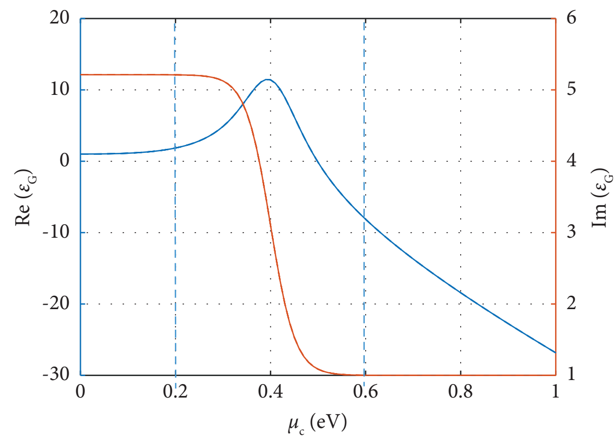

Figure 4: The permittivity (real and imaginary parts) characteristics of graphene versus the chemical potential show three regions: a high absorption region where graphene behaves as a lossy dielectric medium ($\mu_c < 0.2\,\text{eV}$) a transition region ($0.2\,\text{eV} < \mu_c < 0.6\,\text{eV}$) with median absorption suitable for the tuning process and a region of low absorption with a linear dependence where graphene behaves as a quasimetallic medium ($\mu_c > 0.6\,\text{eV}$).

2.2. Methods. Nonlinear coupled mode theory (NCMT) was used to compute energy coefficients needed to determine the spectral responses of a maximally flat-response Butterworth filter in the L band from the spectral requirements for DWDM filters (ITU-T grid) [49]. The nonlinear coupled-mode equations were solved in MATLAB software. The design space exploration of the filter geometry enabled us to relate the spectral and the physical parameters of the filter. A material combination was chosen for the waveguide to ensure low (radiation and bending) losses, CMOS compatibility, compactness, a high tunability efficiency as well as athermal and polarization-insensitive behaviour using a mode analysis solver in COMSOL software. An optimized cross-section, a critical radius, and gap distances between ring resonators and between rings and waveguides were determined at this stage. As the study involves simultaneously electromagnetic wave propagation, heat transfer, and electro-optic tuning, a Multiphysics approach was used to investigate those different aspects of the problem to create conditions making the simulation as close to real life as possible. The finite element, beam envelope propagation method was used to solve the electromagnetic problem in the filter model. Simulations were performed on the ideal material combination chosen to build a highly tunable athermal and polarization-insensitiveadd-drop filter. A flow chart of the methodology is given in Figure 5.

3. Results and Discussion

Given the cross-section dimensions that allow fundamental quasi-TE and quasi-TM modes and athermal behavior with high confinement of the fields in the core of the filter waveguides, this step aims to determine the effective index, the group index as well as a critical bending radius that determines the upper limit for bending losses, stress-induced resonance shift, and birefringence in the filter. To select the critical bending radius, the bent waveguide was replaced with an equivalent straight waveguide with coordinate transformation following conformal mapping [22]. The bending loss was computed from the imaginary part of the effective index for radii in the range of 6 to 37.5 μm at 1570 nm. When the waveguide is bent, the effective index turns complex, and its imaginary part is used to estimate the bending loss. A critical bending radius value of 27.5 μm corresponding to a maximum bending loss of 0.0001 dB/cm was used for the device (Figure 6. The results of this study are found in Table 3. A slight difference in effective indices in TE and TM modes has been tolerated as a tradeoff to realize ring resonator-based devices with different materials that are nearly polarization insensitive. The results have shown that a small birefringence coupled with a selected value of $(H - h)/w$ of a trapezoidal cross-section (Figure 2) can minimize the polarization rotation effects on the spectral performances of the filter [50].

Using the serially-coupled ring resonators topology shown in Figure 1, transfer functions of a three-ringresonator-basedadd-drop filter were determined by solving the nonlinear coupled mode equations (7). The design parameters to consider are as follows: a full wave at half maximum (FWHM) bandwidth of 50 GHz and an FSR of 3.7 nm and a resonance wavelength of 1570 nm. We assume that the waveguide cross-section geometry is constrained by the fabrication process, temperature and polarization stability, and an upper limit of bending losses by using COMSOL Multiphysics. The results from (7) were compared to simulation solutions using a finite element method. Figure 7 shows simulation results of flat-top spectrum responses of a third-order Butterworth filter and demonstrates an excellent agreement between the predictions of the nonlinear coupled mode theory (NCMT) and simulation in the frequency domain finite element mode method (FEM) using COMSOL. In this simulation, the graphene response is modeled as a surface electric current through the electrostatics module. However, a loss increment up to 0.8 dB in the passband from 0.51 dB observed during the NCMT simulation is measured in FEM simulation results. This can be explained by different loss contributions from different sections of the filter, especially polarization losses and coupling losses at the interfaces between microrings and between microrings and bus waveguides. The gap distances are related to the field coupling coefficients given in Table 2 where we notice a slight

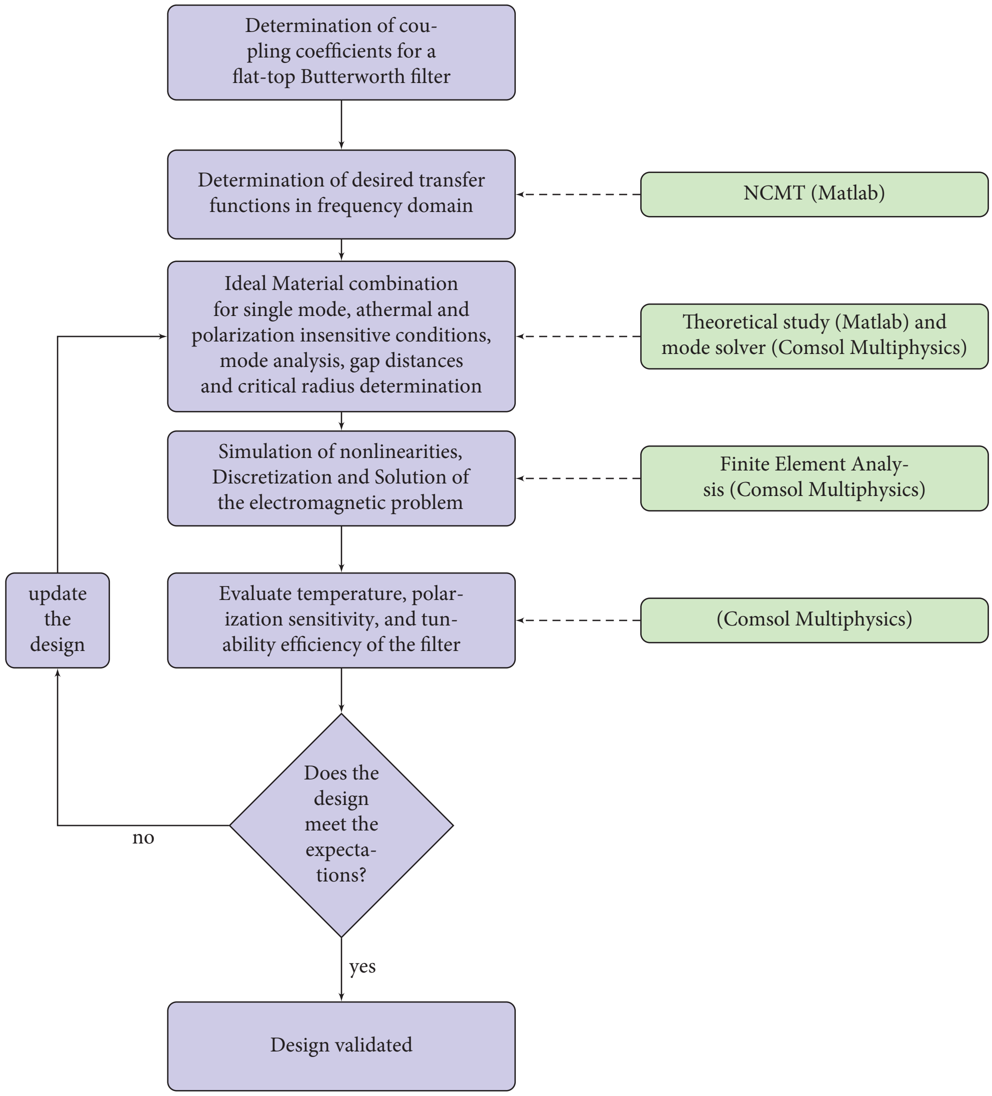

Figure 5: Flow chart of the methodology.

difference in TE and TM modes values, due to the small birefringence in the material system.

The confinement of the field in the straight waveguide depends on the choice of the materials, the waveguide cross-section engineering, together with the operating wavelength range. With a bent waveguide, particular attention was put on the determination of the critical radius to keep the field confined in the center of the core, or equivalently, to reduce the bending losses (Figure 6). Additionally, there is a correlation between the critical radius and the induced stress in the waveguide that can contribute to additional fluctuations of resonant wavelength. In the ring resonators, only wavelengths such that $2\pi R = m(\lambda/n_{\text{eff}})$, where m is an integer and n_r is the effective index of the microring, will propagate through the filter structure and exit at the drop port. Therefore, a sweep-step study is performed on the L band wavelength range to determine wavelengths that satisfy the resonance condition. A value of $\lambda_0 = 1570$ nm was found, and strong field confinement in the filter structure was observed (Figure 8).

To expand the free spectral range (FSR) or equivalently increase the distance between two consecutive resonant wavelengths, a ring resonator with a smaller ring radius is used (Vernier effect). The interstitial resonance amplitudes are lower than 20 dB (7) and thus cannot interfere with other DWDM signals. As a result, the FSR was expanded from 3.7 nm to 18.5 nm, i.e., by a factor of five.

Parameters such as the scattering rate (Γ), the graphene layer thickness (t_G), and the applied voltage (V_G) were analyzed. The increase in the applied voltage induces changes in the transmission spectrum. Wavelength resonance shifting can be observed as long as the breakdown voltage is not reached. The increase in the applied voltage beyond this point is associated with fluctuations of the amplitude response (Figure 9). In the simulated device, the breakdown was observed at the value slightly below 10 V. To investigate the tuning efficiency, the Electrostatics physics was coupled with the Electromagnetic Waves Beam Envelope physics and the simulation results are illustrated in Figures 9 and 10. The simulation results revealed tuning

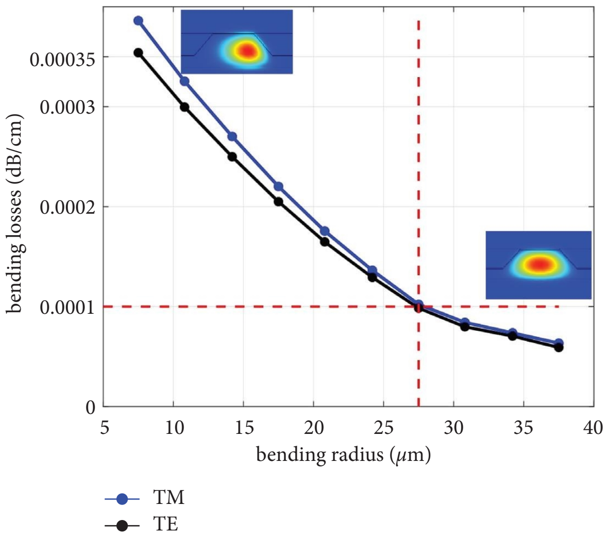

Figure 6: Simulated bending loss as a function of bending radius for TE and TM modes from 6 to 37.5 μm. At a radius of 6 μm, all the mode power radiates from the core. At 37.5 μm, losses are quite similar to those in a straight waveguide. Modes were calculated at a wavelength of 1570 nm. TM mode profiles are included in the figure for bending radii of 6 and 37.5 μm .

Table 3: Mode analysis simulation results on optimal dimensions of the cross-section and an optimal material system enabling athermal and polarization-insensitive behavior of the device.

Mode	n_{eff}	λ (μm)	n_g	Pol ()	A_{eff} (μm^2)
TE	2.2988	1.570	2.6523	96.03	0.204292
TM	2.2971	1.570	2.6515	95.75	0.18388

efficiencies of ~150 pm/V and 21 pm/V over a tuning range of 1.3 nm, with and without the graphene layer, respectively, which confirm the enhancement role of the integrated graphene layer.

A particular attention has been placed on the choice of the electrodes. The material (TiN), size, and location were chosen to transfer efficiently the applied voltage to the ring resonators without altering the optical performance of the filter. As a consequence, the center wavelength was shifted with the applied voltage (Figure 9) as a result of the variation of the refractive and group indices. Figure 11 shows a uniform distribution of the voltage in different microrings. Such a distribution is necessary to ensure a synchronous tuning of individual resonances of the different microrings and will avoid differences with the overall resonance wavelength of the filter.

In this work, the optical filter performance was investigated in the presence of temperature changes. In fact, the thermal variations may result in structural deformation of the filter geometry, i.e., the expansion of the rings' circumference and/or different layers of the filter structure. Thus, the resonant wavelengths may be affected. A temperature gradient of 60 K from the substrate was considered in the study. We assume a situation where the temperature excursion in the filter is consecutive to overheating due to

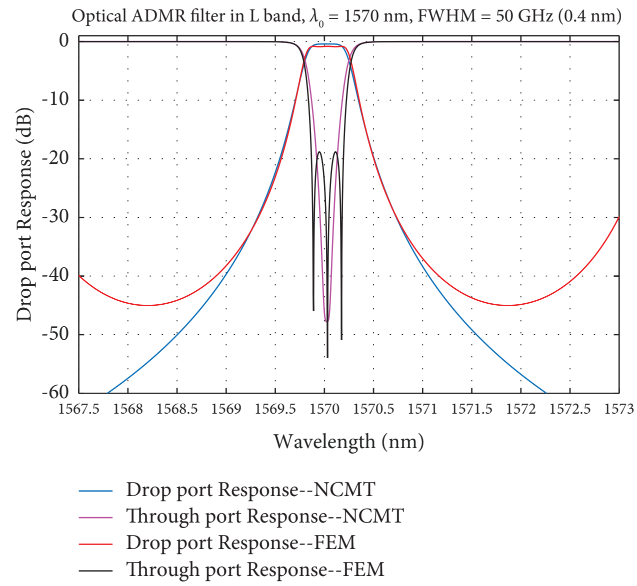

Figure 7: Simulation of the filter responses at through and drop ports using NCMT are plotted together with the S-parameters simulation results given by FEM. $T = 298$ K in the TE mode (TM mode giving practically the same profile). Full wave at half maximum (FWHM) = 50 GHz (0.4 nm) around the resonance wavelength of 1570 nm with FSR = 3.7 nm, $Q = 2584$, finesse = 19, and an extinction ratio (ER) = 60 dB.

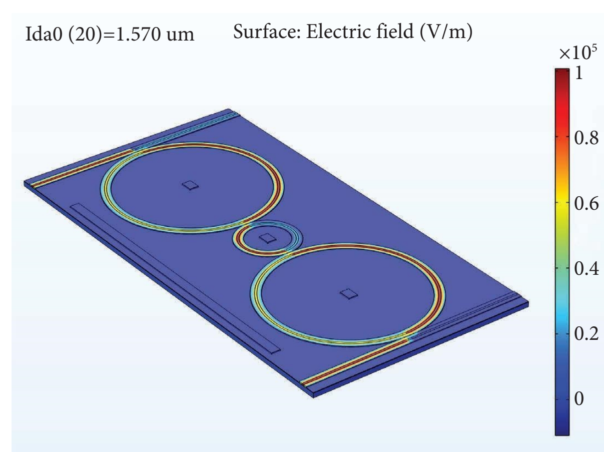

Figure 8: Electric field profile in the filter structure at a resonance wavelength of $\lambda_0 = 1570$ nm. A strong confinement of the electrical field in the structure of the filter is observed, and at resonance, the signal exits at the drop port with very low losses.

power dissipation in the filter itself or in the surrounding components, or simply due to an external heat source. The temperature propagates through the structure from the bottom of the substrate (Figure 12). The figure shows a quasiuniform profile except in joints and in curvatures of the ring resonators. To study their effects on the spectral properties of the filter, Heat Transfer in Solids physics and Solid Mechanics physics coupled to thermal expansion Multiphysics were added to the electromagnetics simulation in the model. The simulation results for temperature and

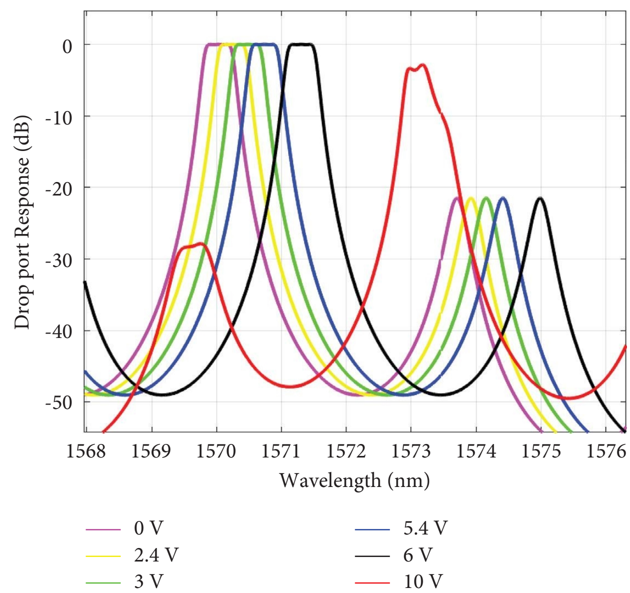

Figure 9: Electro-optically tuned add-drop filter. The thickness and the scattering rate for the graphene layer are $t_G = 3.4$ nm and $\Gamma = 1e14/s$, respectively. The resonance wavelength shifts from the original value of 1570 nm (magenta curve) as a function of the tuning voltage (V_G) varying from 0 to 12 V. The fluctuations in the amplitude response are observed beyond the breakdown voltage (red curve).

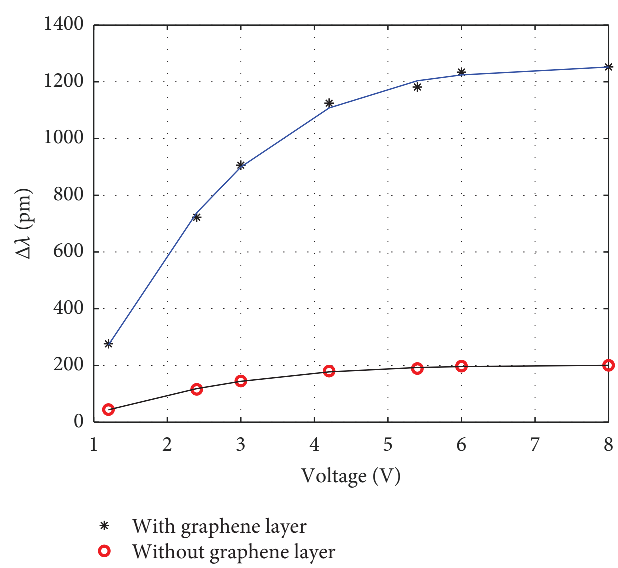

Figure 10: Tuning efficiency evaluation. The resonant wavelength shifts as a function of the applied DC voltage with nonlinear behavior.

stress distributions are given in Figures 12 and 13, respectively. We observed that these effects did not distort the quasifundamental TE and TM modes of the filter at resonance but induced a slight shift of the S-parameters (Figure 14). The overall thermal effects over a gradient of 60 K (within a temperature range from 25 to 85°C) are a 19 pm-resonance shift, thereby temperature stability of 0.3 pm/K.

Thermo-optic effects on the filter are not significant due to the athermal condition imposed by the choice of the material system used. However, the mismatch of coefficients of thermal expansions of different layers in the structure of the filter and particularly the expansion in ring resonators (stress-optical effects) explain the slight resonant wavelength detune. Figure 14 shows a slight shift in the center wavelength and a small increase of loss in the passband (0.1 dB). However, these changes do not affect the performance of the filter for DWDM systems.

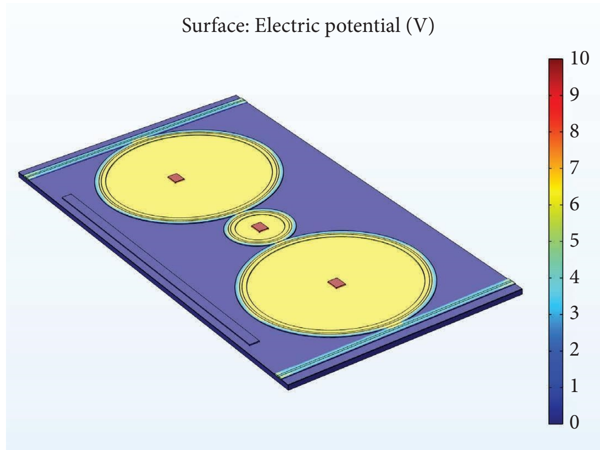

Figure 11: 3D view of the voltage distribution in TiN CMOS-compatible electrodes. The uniform distribution of the electric potential ensures a synchronous tuning of individual resonances in microrings.

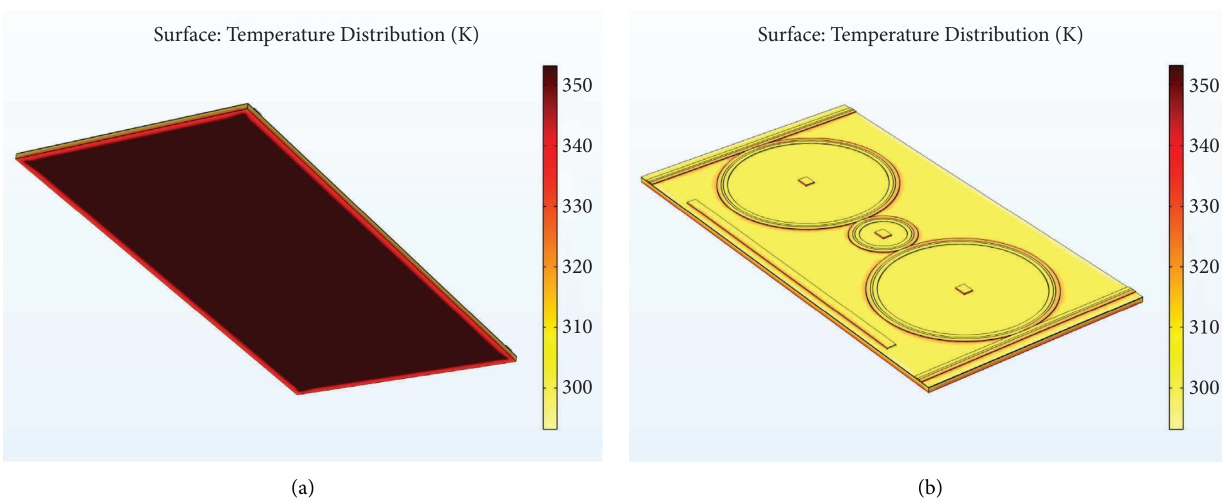

Figure 12: (a) Heat distribution at the bottom of the substrate. (b) 3D view of the heat profile in the structure of the device.

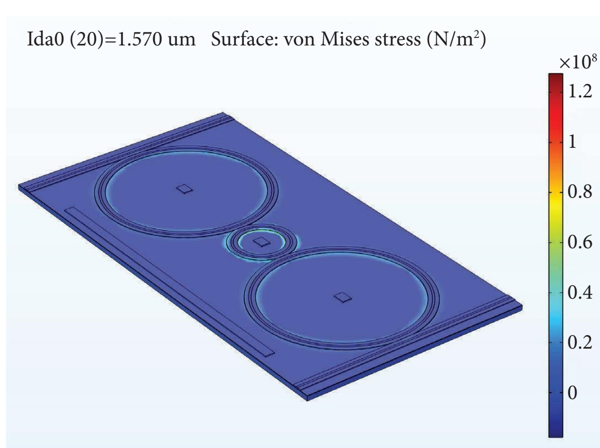

Figure 13: Von Mises stress distribution in the filter due to the heat expansion.

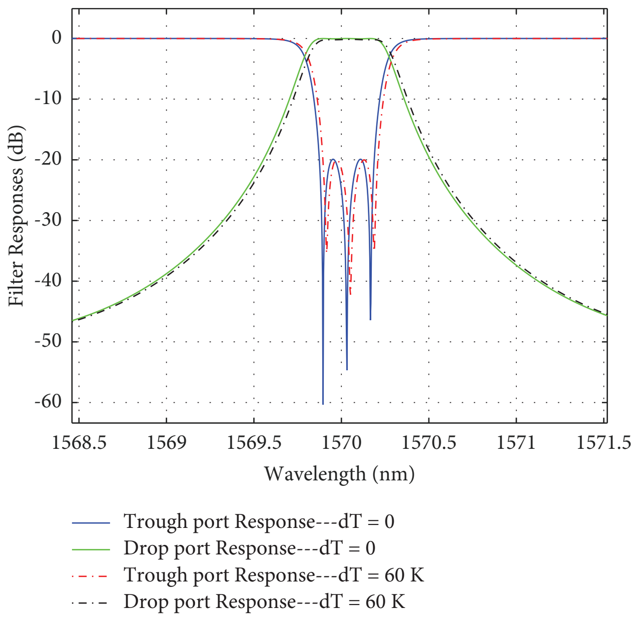

Figure 14: Filter response affected by a heat source from the bottom of the substrate of the filter (thermo-optic effects) and thermal deformation (stress-optic effects).

These results enabled us to state that particular attention should be put on the choice of the material system, the computation of the cross-section dimensions, the size of different layers, and the ring resonator bending radius.

4. Conclusion

This work investigated the athermality, polarization-insensitivity, and tunability of an add-drop filter based on ring resonators for DWDM systems. Using a 3D Multiphysics approach, the main goal was to relate the spectral parameters specified by the ITU-grid for DWDM systems and the material, physical, and optical parameters of an athermal, polarization insensitive, and tunable filter. The results demonstrate an innovative tunable filter exploiting nonlinearities in silicon-rich nitride enhanced by a graphene layer on top of the core material. We found that the electro-optically tunable filter can arbitrarily operate with TM and TE polarized signals in the less occupied L band (1565 nm–1625 nm) with high thermal stability (0.3 pm/K) and without interference with neighbouring DWDM channels on a range of 18.5 nm.

In the future, this research intends to consider all-optical tuning methods and compare the performance with the electro-optical method used in the work for modern DWDM systems.

Data Availability

This is to state that data supporting the results will be made available on request through the corresponding author (Filston Rukerandanga, filston2006@gmail.com).

Disclosure

The study is part of the academic requirements for a Ph.D. degree.

Conflicts of Interest

The authors declare that they have no conflicts of interest.

Acknowledgments

The authors thank the African Union Commission for Education for granting the software facilities to make the simulations and the Kenya Education Network (KENET) for granting the simulation facilities (remote High-Performance Virtual PC).

References

[1] A. N. R. Ahmed, S. Shi, M. Zablocki, P. Yao, and D. W. Prather, "Tunable hybrid silicon nitride and thin-film lithium niobate electro-optic microresonator," *Optics Letters*, vol. 44, no. 3, pp. 618–621, 2019.

[2] M. Teng, S. Fathpour, R. Safian et al., "Miniaturized silicon photonics devices for integrated optical signal processors," *Journal of Lightwave Technology*, vol. 38, no. 1, pp. 6–17, 2020.

[3] D. Liu, C. Zhang, Di Liang, and D. Dai, "Submicron-resonator-basedadd-drop optical filter with an ultra-large free spectral range," *Optics Express*, vol. 27, no. 2, pp. 416–422, 2019.

[4] S. Dey, "Optical hextuple ring resonator-based delay line architecture," *Journal of Optics*, vol. 51, no. 1, pp. 106–114, 2022.

[5] G. K. Bharti and R. K. Sonkar, "Implementation of polarization rotation using microring resonator and its application to design all-optical switch," *Optical Engineering*, vol. 60, no. 8, Article ID 085109, 2021.

[6] D. Liu, J. Tang, Y. Meng, W. Li, N. Zhu, and M. Li, "Ultra-low v pp and high-modulation-depthinp-based electro–optic microring modulator," *Journal of Semiconductors*, vol. 42, no. 8, Article ID 082301, 2021.

[7] A. Pasquazi, M. Peccianti, L. Razzari et al., "Micro-combs: a novel generation of optical sources," *Physics Reports*, vol. 729, no. 1–81, pp. 1–81, 2018.

[8] Y. Tan and D. Dai, "Silicon microring resonators," *Journal of Optics*, vol. 20, no. 5, Article ID 054004, 2018.

[9] Y. R. Bawankar and A. Singh, "Microring resonators based applications in silicon photonics-a review," in *Proceedings of the 2021 5th Conference on Information and Communication Technology (CICT)*, IEEE, Kurnool, India, December 2021.

[10] M. Bahadoran, "Analysis of ingaasp-inp double microring resonator using signal flow graph method," *Journal of Optoelectronical Nanostructures*, vol. 3, no. 2, pp. 41–52, 2018.

[11] C. Sun, X. Liu, B. Xiong et al., "Microwave photonic devices based on high-q aln microring resonators," in *Proceedings of the Asia Communications and Photonics Conference*, Optical Society of America, Washington, D.C., United States, June 2017.

[12] I. Amiri, R. Zakaria, T. Anwar, M. Bahadoran, D. Vigneswaran, and P. Yupapin, "Dual wavelength optical duobinary modulation using gaas–algaas microring resonator," *Results in Physics*, vol. 11, pp. 1087–1093, 2018.

[13] M. Ariannejad, I. Amiri, S. R. B. Azzuhri, R. Zakaria, and P. Yupapin, "Polarization dependence of su-8 micro ring resonator," *Results in Physics*, vol. 11, pp. 515–522, 2018.

[14] P. Jean, A. Douaud, T. Thibault, S. LaRochelle, Y. Messaddeq, and W. Shi, "Sulfur-rich chalcogenide claddings for athermal and high-q silicon microring resonators," *Optical Materials Express*, vol. 11, no. 3, p. 913, 2021.

[15] M. Bahadori, K. Bergman, M. Nikdast et al., "Design space exploration of microring resonators in silicon photonic interconnects: impact of the ring curvature," *Journal of Lightwave Technology*, vol. 36, no. 13, pp. 2767–2782, 2018.

[16] T. Verolet, A. Gallet, X. Pommarède, J. Decobert, and D. Make, "Hybrid iii-v on silicon fast and widely tunable laser based on rings resonators with pin junctions," in *Proceedings of the 2018 Asia Communications and Photonics Conference (ACP)*, IEEE, Hangzhou, China, October 2018.

[17] M. Chen, Li Liu, L. Xu, M. Ye, X. Jin, and Z. Yu, "On-chipall-optical tunable filter with high tuning efficiency," *IEEE Photonics Journal*, vol. 12, no. 2, pp. 1–10, 2020.

[18] H. Han and B. Xiang, "Simulation and analysis of electro-optic tunable microring resonators in silicon thin film on lithium niobate," *Scientific Reports*, vol. 9, no. 1, p. 6302, 2019.

[19] T. Hu, W. Wang, C. Qiu et al., "Thermally tunable filters based on third-order microring resonators for wdm applications," *IEEE Photonics Technology Letters*, vol. 24, no. 6, pp. 524–526, 2012.

[20] X. Liu, P. Ying, X. Zhong et al., "Highly efficient thermo-optic tunable micro-ring resonator based on an lnoi platform," *Optics Letters*, vol. 45, no. 22, pp. 6318–6321, 2020.

[21] J. S. Fandiño, P. Muñoz, D. Doménech, and J. Capmany, "A monolithic integrated photonic microwave filter," *Nature Photonics*, vol. 11, no. 2, pp. 124–129, 2017.

[22] K. Alan Vey Van, *Optical Microring Resonators: Theory, Techniques, and Applications*, CRC Press, Taylor et Francis Group, Boca Raton, FL, 2018.

[23] M. AlAloul and M. Rasras, "Plasmon-enhanced graphene photodetector with cmos-compatible titanium nitride," *Journal of the Optical Society of America B*, vol. 38, no. 2, pp. 602–610, 2021.

[24] C.-L. Wu, Y.-Jr Hung, R. Fan et al., "Tantalum pentoxide (ta2o5) based athermal micro-ring resonator," *OSA Continuum*, vol. 2, no. 4, p. 1198, 2019.

[25] M. L. Vermeer, N. K. Alhareeb, H. K. Trieu, and T. Lipka, "Athermal electro-optic trimmable waveguide design," *MikroSystemTechnik Congress 2021; Congress*, vol. 1, 2021.

[26] F. Dell'Olio, D. Conteduca, G. Brunetti, M. N. Armenise, and C. Ciminelli, "Novel CMOS-compatible athermal and polarization-insensitive ring resonator as photonic notch filter," *IEEE Photonics Journal*, vol. 10, no. 6, pp. 1–11, 2018.

[27] S. Namnabat, K.-Jo Kim, A. Jones et al., "Athermal silicon optical add-drop multiplexers based on thermo-optic coefficient tuning of sol-gel material," *Optics Express*, vol. 25, no. 18, p. 21471, 2017.

[28] V. Mere, R. Kallega, and S. K. Selvaraja, "Efficient and tunable strip-to-slot fundamental mode coupling," *Optics Express*, vol. 26, no. 1, pp. 438–444, 2018.

[29] L. Leick, K. Zenth, C. Laurent-Lund, T. Koster, L. Wang, and B. H. Larsen, "Low loss, polarization insensitive sion components," in *Proceedings of the Optical Fiber Communication Conference, page MF40*, Optical Society of America, Los Angeles, CA, USA, December 2004.

[30] H. Wang, J. Dai, H. Jia et al., "Polarization-independent tunable optical filter with variable bandwidth based on silicon-on-insulator waveguides," *Nanophotonics*, vol. 7, no. 8, pp. 1469–1477, 2018.

[31] Pu Zhang, H. Huang, Y. Jiang et al., "High-speedelectro-optic modulator based on silicon nitride loaded lithium niobate on an insulator platform," *Optics Letters*, vol. 46, no. 23, p. 5986, 2021.

[32] A. Pandya, V. Sorathiya, and S. Lavadiya, "Graphene-based nanophotonic devices," in *Recent Advances in Nanophotonics*, M. Kahrizi and P. A. Sohi, Eds., Rijeka, 2020.

[33] K. J. A. Ooi, P. C. Leong, L. K. Ang, and D. T. H. Tan, "All-optical control on a graphene-on-silicon waveguide modulator," *Scientific Reports*, vol. 7, no. 1, p. 12748, 2017.

[34] V. G. Ataloglou, T. Christopoulos, and E. E. Kriezis, "Nonlinear coupled-mode-theory framework for graphene-induced saturable absorption in nanophotonic resonant structures," *Physical Review A*, vol. 97, no. 6, Article ID 063836, 2018.

[35] Z. Bao, Y. Tang, Z.-Da Hu et al., "Inversion method characterization of graphene-based coordination absorbers incorporating periodically patterned metal ring metasurfaces," *Nanomaterials*, vol. 10, no. 6, p. 1102, 2020.

[36] D. Conteduca, F. Dell'Olio, C. Ciminelli, and M. N. Armenise, "Resonant graphene-based tunable optical delay line," *IEEE Photonics Journal*, vol. 7, no. 6, pp. 1–9, 2015.

[37] D. Bonneau, J. W. Silverstone, and M. G. Thompson, *Silicon Quantum Photonics III: Systems and Applications*, Springer, Berlin, Heidelberg, 2016.

[38] J. Wang, Li Fan, L. T. Varghese et al., "A theoretical model for an optical diode built with nonlinear silicon microrings," *Journal of Lightwave Technology*, vol. 31, no. 2, pp. 313–321, 2013.

[39] D. T. H. Tan, K. J. A. Ooi, and D. K. T. Ng, "Nonlinear optics on silicon-rich nitride—a high nonlinear figure of merit cmos platform," *Photonics Research*, vol. 6, no. 5, pp. B50–B66, 2018.

[40] Q. Feng, H. Cong, B. Zhang et al., "Enhanced optical kerr nonlinearity of graphene/si hybrid waveguide," *Applied Physics Letters*, vol. 114, no. 7, Article ID 071104, 2019.

[41] H. Cong, F. Qi, J. Zhang, and L. Chen, "Optical kerr nonlinearity of cmos compatible pecvd deposited si-rich-nitride (srn)," in *Proceedings of the 2019 IEEE 16th International Conference on Group IV Photonics (GFP)*, IEEE, NY China, June 2019.

[42] V. Van, "Circuit-based method for synthesizing serially coupled microring filters," *Journal of Lightwave Technology*, vol. 24, no. 7, pp. 2912–2919, 2006.

[43] A. Melloni and M. Martinelli, "Synthesis of direct-coupled-resonators bandpass filters for WDM systems," *Journal of Lightwave Technology*, vol. 20, no. 2, pp. 296–303, 2002.

[44] H. Venghaus, *Wavelength Filters in Fibre Optics*, Springer Series in optical sciences, Heidelberg, Germany, 2007.

[45] S. Miller, H. Yoon, D. Lee, J. Cardenas, and L. Alexander, "Gaeta and michal lipson. "Electro-optic effect in silicon nitride," in *Proceedings of the Conference on Lasers and Electro-Optics Europe - Technical Digest*, Beijing China, August 2015.

[46] J. Čtyroký, J. Petráček, P. Kwiecien, I. Richter, and V. Kuzmiak, "Graphene on an optical waveguide: comparison of simulation approaches," *Optical and Quantum Electronics*, vol. 52, no. 3, p. 149, 2020.

[47] Y. Yi, P. Pignalosa, and D. Wu, "Tunable and ultra-small graphene integrated silicon racetrack micro resonator," *IEEE Journal of Selected Topics in Quantum Electronics*, vol. 23, no. 1, pp. 173–178, 2017.

[48] Y. Wang, L. Lei, J. Zang, W. Dong, X. Zhang, and P. Xu, "High efficiency electro-optic modulation in a graphene silicon hybrid tapered microring resonator," *IEEE Access*, vol. 9, pp. 87869–87876, 2021.

[49] T. G. Itu, "Spectral grids for WDM applications: DWDM frequency grid," *Serie Geologica*, vol. 694, no. 1, 2012.

[50] F. Morichetti, A. Melloni, and M. Martinelli, "Effects of polarization rotation in optical ring-resonator-based devices," *Journal of Lightwave Technology*, vol. 24, no. 1, pp. 573–585, 2006.